CMS Physics Analysis Summary

Contact: cms-pag-conveners-higgs@cern.ch 2015/05/05

Search for H/A decaying into Z and A/H, with Z$\to \ell\ell$ and A/H$\to$ bb or A/H$\to \tau\tau$

The CMS Collaboration

Abstract

A search is performed for a new heavy resonance decaying to a Z boson and a light resonance, where the light resonance decays to either a pair of bottom quarks or a pair of tau leptons and the Z boson decays to two electrons or two muons. The search exploits a data sample collected during 2012 by the CMS experiment at the center-of-mass energy of $\sqrt{s} = 8$ TeV and corresponding to an integrated luminosity of $\mathcal{L}$ = 19.8 fb^{-1}. No significant deviation from the standard model expectations is observed and limits are set on benchmark production processes predicted in a model with two Higgs doublets.

1 Introduction

The observation of a new particle with a mass of about 125 GeV was reported by the ATLAS and CMS experiments at the LHC in the WW, ZZ and $\gamma\gamma$ final states [1, 2]. Evidence of the decay of the particle to pairs of fermions ($\tau\tau$ and $b\bar{b}$) was also reported later [3]. The measurements of mass, branching ratios, production rates, spin and parity are all consistent with the predictions of the standard model (SM), where a single doublet of Higgs fields is present. The existence of additional Higgs bosons is however predicted in simple extensions of the SM scalar sector, like models with two Higgs doublets (2HDM) [4]. These models predict the existence of five physical Higgs particles that arise as a consequence of the electroweak symmetry breaking mechanism: two neutral CP-even scalars (h, H), one neutral CP-odd pseudoscalar (A), and two charged scalars (H^+, H^-).

One important motivation for 2HDMs is that these models provide a way to explain the asymmetry between matter and anti-matter observed in the Universe [4, 5]. Another important motivation is Supersymmetry [6], which is a theory that falls in the broad class of 2HDMs. Axion models [7], which would explain how the strong interaction does not violate the CP symmetry, would give rise to an effective low-energy theory with two Higgs doublets. Finally, it has also been recently noted [8] that certain realizations of 2HDMs can accommodate the muon $g-2$ anomaly [9] without violating the present theoretical and experimental constraints.

In the most general case 14 parameters are necessary to describe the scalar sector in a 2HDM. However, only 6 free parameters remain once the so-called Z_2 symmetry is imposed to suppress flavor changing neutral currents, in agreement with experimental observations, and the values of the mass of the recently discovered Higgs boson (125 GeV) and the electroweak vacuum expectation value (246 GeV) are assumed. The compatibility of a 125 GeV SM-like Higgs boson with 2HDMs is possible in the so-called alignment limit. In such a limit, one of the CP-even scalars, h or H, is identified with the 125 GeV Higgs boson and the condition $cos(\beta-\alpha) \approx 0$ or $sin(\beta-\alpha) \approx 0$ is satisfied, where $\tan\beta$ and α are, respectively, the ratio of the vacuum expectation values, and the mixing angle of the two Higgs doublets. A recent theoretical study [5] has shown that, in this limit, a large mass splitting (>100 GeV) between the A and H bosons would favor the electroweak phase transition that would be at the origin of the baryogenesis process in the early Universe, thus explaining the currently observed matter-antimatter asymmetry in the Universe. In such a scenario, the most frequent decay mode of the pseudoscalar A boson would be A$\rightarrow$ZH.

In this document a search for a new resonance decaying to a Z boson and a lighter resonance is described. Two different searches are performed, targeting the decay of the lighter resonance in either a pair of tau leptons or a pair of b-quarks. In both cases the Z boson is identified via its decay into either a pair or electrons or a pair of muons. Since the analysis strategy adopted is independent from the assumed model and spin, the results can be also interpreted in the specular topology H$\rightarrow$ZA, where the expected 2HDM mass hierarchy is inverted and the pseudoscalar A is predicted to be light. Throughout the text, the symbol ℓ refers to an electron or a muon. Concerning the $\ell\ell\tau\tau$ channel, the following leptonic and hadronic di-tau final states are considered: $e\mu$, $e\tau_h$, $\mu\tau_h$ and $\tau_h\tau_h$, where τ_h indicates a hadronically-decaying tau. The choice of bb and $\tau\tau$ final states is motivated by the large branching fractions predicted in most of the 2HDM phase space.

The reconstruction and selection of the main physics objects involved in the final state is described in Section 4. The background estimation is based on data control regions whenever possible and is explained in Section 5. The evaluation of the experimental and theoretical systematic uncertainties relevant for this search is reported in Section 6. Finally, the results of the

search are reported in Section 7.

2 The CMS detector

The central feature of the CMS apparatus is a superconducting solenoid of 6 m internal diameter, providing a magnetic field of 3.8 T. Within the superconducting solenoid volume a silicon pixel and strip tracker, a lead tungstate crystal electromagnetic calorimeter (ECAL), and a brass and scintillator hadron calorimeter (HCAL), each composed of a barrel and two endcap sections, are located in concentric layers. These layers provide coverage out to a pseudorapidity $|\eta| = 2.5$. Together with the magnet, the tracking system allows for tracks with transverse momentum p_{T} as low as 100 MeV to be reconstructed, and give a p_{T} resolution of 1% at 100 GeV. The ECAL electromagnetic transverse energy resolution is of about $3\%/\sqrt{E_T/\,\mathrm{GeV}}$, and the HCAL transverse hadronic energy resolution is of about $100\%/\sqrt{E_T/\,\mathrm{GeV}}$. Muons are measured in gas-ionization detectors embedded in the steel flux-return yoke outside the solenoid. Extensive forward calorimetry complements are provided by the barrel and endcap detectors up to $|\eta| < 5.2$. The first level (L1) of the CMS trigger system uses information from the calorimeters and muon detectors to select the most interesting events in a fixed time interval of less than 4 μs. The high-level trigger (HLT) processor farm further decreases the event rate from around 100 kHz to around 400 Hz before data storage. A more detailed description of the CMS detector, together with a definition of the coordinate system used and the relevant kinematic variables, can be found in Ref. [10].

3 Data and simulation samples

The data were collected during 2012 at the center-of-mass energy of $\sqrt{s} = 8$ TeV, for a total luminosity of $\mathcal{L} = 19.8$ fb^{-1}. The average number of interactions per bunch crossing (pileup) in the considered data sample was 21. Events are selected using di-electron and di-muon triggers [11, 12]. The di-lepton triggers have transverse momentum (p_{T}) thresholds of 17 and 8 GeV, and loose identification and isolation criteria.

Simulated events corresponding to the main background processes, W/Z+jets, $\mathrm{t\bar{t}}$ +jets, diboson, are generated with MADGRAPH 5 [13] whereas PYTHIA 6 [14] was used for the parton showering. In addition for the $\tau\tau$ channel the SM background contribution from ZZ production via the $q\bar{q}$ initial states is generated at Next-to-Leading Order (NLO) with POWHEG [15]. The same is done for the single-top production process. The detector response is simulated using a detailed description of the CMS detector, based on the GEANT4 toolkit [16]. The simulated samples include a number of pileup collision events reflecting the distribution measured in the data. The "tag and probe" technique [17] is used to correct the simulation results.

In the context of the 2HDM, two processes have been considered as signal: H$\rightarrow$ZA and A$\rightarrow$ZH where the pseudo-scalar A and the scalar H, respectively, decay to $\tau\tau$ or bb, and the Z decays to $\ell\ell$. The latest MADGRAPH 5 version, interfaced with PYTHIA 6 and TAUOLA [18], has been used to generate different signal processes according to different M_A and M_H combinations. The signal samples have been obtained using the full simulation and reconstruction chain within the CMSSW official framework. Considering the parameter space still allowed by direct searches, the chosen values for $\cos(\beta - \alpha)$ and $\tan\beta$ are 0.01 and 1.5, respectively. The lightest scalar has the same properties as the SM Higgs boson and its mass M_h has been fixed at 125 GeV. The masses of the charged Higgs bosons ($M_H^{\pm}$) are set equal to the highest mass involved in the signal process (M_H or M_A) in order to preserve the degeneracy $M^2_{H^{\pm}} \sim M^2_{H/A}$. The production

cross section values, used in the normalization of the signal samples, are extracted from the SusHi program [19], which provides the Next-to-Next-to-Leading-Order (NNLO) predictions.

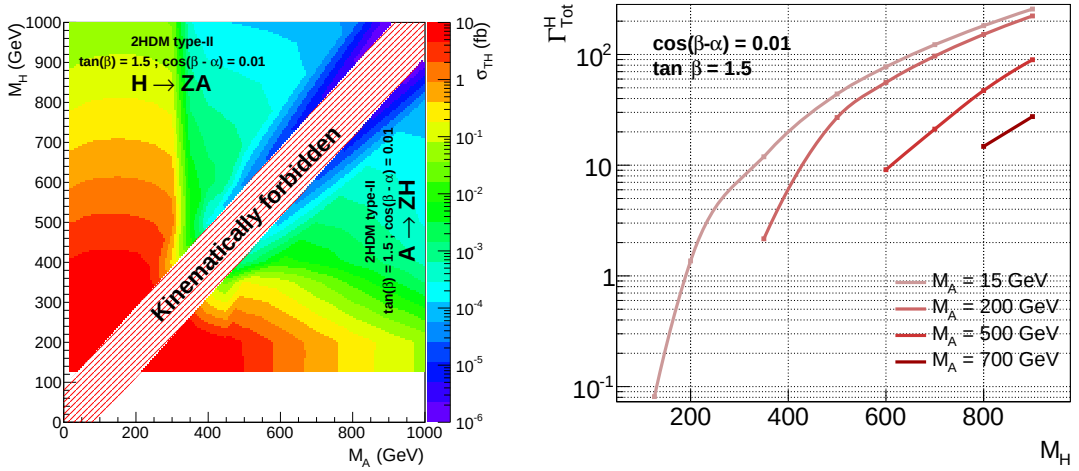

(a) (b)

Figure 1: Left: cross section times branching ratio values for the processes H/A→ZA/H→ $\ell\ell\tau\tau$ (in fb) normalized to NNLO SusHi predictions. Right: widths of heavy H for some representative signal benchmark points for different mass values of the pseudo-scalar A decaying into a pair of b-jets. The chosen model parameters, $\cos(\beta-\alpha)$= 0.01 and $\tan\beta$ = 1.5, are reported on both figures.

Figure 1a shows the NNLO theoretical cross-sections times branching ratios ($\sigma \cdot BRs$) in the plane M_H-M_A for the process $H \to ZA \to \ell\ell\tau\tau$ in the upper left triangle, and the process $A \to ZH \to \ell\ell\tau\tau$ in the bottom right triangle. The $\sigma \cdot BRs$ for the signal samples used in the $\ell\ell\tau\tau$ analysis correspond to values of $M_{H/A}$ and $M_{A/H}$ varying in the ranges [200,1000] GeV and [15,900] GeV, respectively, with the constraint $M_{H/A} > M_{A/H} + M_Z$. The region where M_H is smaller than M_h is not allowed in the considered model. In the case of the $A/H \to$ bb decay channel, a homogeneous set of signal mass points in the M_H-M_A plane is also simulated to study the kinematics and the width of the resonant Higgs bosons. These specific mass points have been generated with MADGRAPH 5 and interfaced with the DELPHES [20] fast simulation framework, tuned for delivering with good approximation the CMS performance in the reconstruction of physics objects. The order of magnitude of the expected signal widths, for the mass range considered in this search, is shown in Fig. 1b.

4 Event reconstruction and selection

The search in both channels, $\ell\ell$bb and $\ell\ell\tau\tau$, is based on the standard CMS analysis framework [21].

The object reconstruction is based on the particle-flow (PF) algorithm [22–24], which combines information from all CMS subdetectors to identify and reconstruct individual particles in the event: muons, electrons, photons, charged and neutral hadrons. From the resulting particle list, jets, taus decaying hadronically and missing transverse energy (E_T^{miss}), defined as the magnitude of the vector sum of the transverse momenta of all observed bodies, are clustered. In order to minimize the effect of the pileup interactions, particles are required to originate from

the primary vertex. The primary vertex, reconstructed with the Deterministic Annealing algorithm [25], is the one characterized by the largest quadratic sum of the p_T of its constituent tracks.

Muons are identified by performing a combined fit to position measurements from both the inner tracker and the muon detectors [26]. Electrons are identified by combining tracks and electromagnetic calorimeter clusters, including the energy deposits from final state radiation [27]. Hadronically-decaying taus are reconstructed and identified using the "hadron-plus-strips" algorithm [28] which uses charged hadrons and photons to reconstruct the main decay modes of the tau lepton: one charged hadron, one charged hadron plus photons, and three charged hadrons. Electrons and muons misidentified as hadronic taus are suppressed using dedicated criteria based on the consistency between the measurements in the tracker, the calorimeters, and the muon detector.

To reject non-prompt or misidentified leptons, electrons, muons, and taus are required to satisfy isolation criteria based on either the absolute or relative isolation variables. The absolute lepton isolation is defined as:

$$I_{\text{abs}} = \sum_{\text{CH}} p_{\text{T}} + \max\left(\sum_{\text{NH}} p_{\text{T}} + \sum_{\gamma} p_{\text{T}} - 0.5 \cdot \sum_{\text{CH,PU}} p_{\text{T}}, 0\right) \quad (1)$$

In this formula, $\sum_{\text{CH}} p_{\text{T}}$ is the scalar sum of the transverse momenta of the charged hadrons originating from the primary vertex and located in a cone of size $\Delta R = \sqrt{(\Delta\eta)^2 + (\Delta\phi)^2}$ =0.4 (0.3) with the axis centered on the muon (electron) direction. All the other sums in the formula, $\sum_{\text{NH}} p_{\text{T}}$ and $\sum_{\gamma} p_{\text{T}}$, represent the same quantity for neutral hadrons and photons, respectively. Concerning taus, the particles used in the reconstruction of the object are excluded from the sums. The term $\sum_{\text{CH,PU}} p_{\text{T}}$ is the contribution of pileup photons and neutral hadrons estimated by using the scalar sum of the transverse momenta of charged hadrons from pileup vertices in the cone. The factor 0.5 corresponds to an estimated average of neutral to charged particles produced in the hadronization process and is measured using simulated events. The relative isolation is defined as $I_{\text{rel}} = I_{\text{abs}}/p_{\text{T}}$, where p_{T} is the lepton transverse momentum.
Jets are reconstructed using the FASTJET software package from all the particle flow candidates according to the AK5 algorithm [29] with a distance parameter of radius 0.5. As part of the jet clustering procedure, charged PF particles not associated with the primary vertex are excluded by means of the Charged Hadron Subtraction technique (CHS). The identification of b-tagged jets is done via the Combined Secondary Vertex (CSV) algorithm [30], which exploits observables related to the long lifetime of b hadrons. The E_T^{miss}, based on PF reconstructed quantities, contains azimuthal corrections of detector resolution effects.

Despite the same object definition is valid for both $\ell\ell$bb and the $\ell\ell\tau\tau$ final states, the baseline event selections are customized, given the very different backgrounds affecting each channel. The methods for reducing and estimating backgrounds are described separately in the following sections.

4.1 Baseline event selection for $\ell\ell$bb

The Z decay leptons are selected by the following requirements, driven by trigger acceptance and spatial boundaries of the CMS subdetectors: $p_{\text{T}} > 20\,\text{GeV}$, $|\eta| < 2.5$ for electrons and $p_{\text{T}} > 20\,\text{GeV}$, $|\eta| < 2.4$ for muons. The isolation cone of the leptons is taken to be $\Delta R < 0.3$ for electrons and $\Delta R < 0.4$ for muons and the final relative isolation cut is set to $I_{\text{rel}} < 0.15$ for electrons and $I_{\text{rel}} < 0.2$ for muons. Jets are selected to be in the kinematic region $p_{\text{T}} > 30$

GeV and $|\eta| < 2.4$. In the reconstruction and selection of $\ell\ell$bb events the presence of two same-flavor, opposite-sign, and reconstructed lepton candidates forming an invariant mass pair in the range [76,106] GeV is required. This allows to get rid of the contamination of non-resonant Drell-Yan+jets and $t\bar{t}$ background processes. In case of multiple candidates, the lepton pair with the closest invariant mass to the nominal Z mass is chosen [31].

At least two CSV b-tagged jets are required to be present in the event, in order to reduce the contribution of Z+light jets events: these candidates are selected as those with the highest value of the CSV discriminant. The chosen working point (WP) for the b-tagged jets identification is the medium one which corresponds to a b-tagging efficiency greater than 65% and to a misidentification probability of light-parton jets (jets originating from gluons or u, d and s quarks) equal to 1% [30]. The $E_{\mathrm{T}}^{\mathrm{miss}}$ significance ($\mathrm{E}_{\mathrm{T}}^{\mathrm{miss}}$sig) is used to suppress backgrounds originating from $t\bar{t}$ processes. As defined, the significance offers an event-by-event assessment of the likelihood that the observed $E_{\mathrm{T}}^{\mathrm{miss}}$ is consistent with zero given the reconstructed content of the event and known resolutions of the CMS detector. This variable is more discriminating against the $t\bar{t}$ process than the $E_{\mathrm{T}}^{\mathrm{miss}}$ itself and, at the same time, leads to smaller systematic uncertainties. The $E_{\mathrm{T}}^{\mathrm{miss}}$ significance is required to be less than 10.

4.2 Baseline event selection for $\ell\ell\tau\tau$

As for the $\ell\ell$bb channel, the Z decay leptons are selected by requiring $p_{\mathrm{T}} > 20\,\mathrm{GeV}$, $|\eta| < 2.5$ for electrons and $p_{\mathrm{T}} > 20\,\mathrm{GeV}$, $|\eta| < 2.4$ for muons. The isolation cut chosen for light leptons is I_{rel} <0.3. The reconstructed invariant mass of the two leptons is required to be in the range [76,106] GeV. Additionally, a Z p_{T} >20 GeV and a difference in the azimuthal angle between the Z and $E_{\mathrm{T}}^{\mathrm{miss}}$ greater than 1.5 are required to suppress the Z+jets background.

In addition to the two light leptons required to reconstruct the Z, two additional opposite sign and different flavour leptons (e, μ and τ) are required to reconstruct the H/A candidate. The requirements on the pseudorapidity and the relative isolation for the light leptons are the same as for the Z decay leptons, while the p_{T} is required to be greater than 10 GeV. Tau candidates with well reconstructed decay modes and fulfilling the criteria to reject electrons and muons reconstructed as hadronic taus are required to have $p_{\mathrm{T}} > 20\,\mathrm{GeV}$ and $|\eta| < 2.3$. The absolute tau isolation required is $I_{\mathrm{abs}} < 2\,\mathrm{GeV}$. For all the mass points and channels, lepton isolation values have been set according to an optimization procedure aimed at maximizing the *a priori* expected significance.

The Z+jets background is further reduced by selecting events with high L_T, where L_T indicates the scalar sum of the visible p_T of the two objects coming from the decay of the $\tau\tau$ pair. Maximizing the a priori expected significance, the optimal requirement on the L_T quantity is found for each mass point and for each final state independently, by scanning the cut threshold between 0 and 200 GeV with steps of 20 GeV.

Jets are required to have $p_{\mathrm{T}} > 30\,\mathrm{GeV}$ and $|\eta| < 4.7$. However, to reject the large $t\bar{t}$ background, all the events with at least on jet with p_T >20 GeV and $|\eta| < 2.4$, and tagged as b-jet by passing the medium working point for the CSV discriminator are vetoed.

In order to exploit the visible and the invisible information related to the τ decays, the Secondary Vertex Fit algorithm (SVFit) [32] is used to calculate the di-tau mass. The SVFit algorithm is a likelihood-based method that combines the reconstructed $E_{\mathrm{T}}^{\mathrm{miss}}$ and its resolution with the momentum of the visible tau decay products in order to obtain a precise estimator of the mass of the parent particle.

Muon momentum scale corrections [12] and electron energy corrections [33] also applied to

both $\ell\ell$bb and $\ell\ell\tau\tau$ analyses, for a better data-simulation agreement in the kinematics of the leptons.

5 Background estimation

5.1 The $\ell\ell$bb channel

After the event selection described in Section 4 for reconstructing the $\ell\ell$bb final state, a significant deviation of data from the MC predictions is observed in the distribution of the $M_{\ell\ell\text{bb}}$ mass, mostly localized in the region 400-700 GeV. A reweighting technique is therefore applied, in order to correct possible mis-modelling of the LO Drell-Yan sample used in the simulation, which might affect the final results. The ratio NLO/LO of the light and heavy flavor component of the $M_{\ell\ell\text{jj}}$ distribution is fit with a third order polynomial and separate reweighting for these two categories is performed. A systematic on this reweighting is also assigned, as discussed in Section 6.

The relevant sources of background for the $\ell\ell$bb final state originate from Z + b-tagged jets processes, $\text{t}\bar{\text{t}}$ pair production, double vector bosons production, and vector boson associated production with a SM Higgs boson. Contributions like ZZ, WW, WZ, and tW have been normalized to the CMS measurement [34–37]. The associated production of Z with the Higgs-like scalar boson (Zh) is also accounted as a background and normalized to the expected theoretical cross section [38]. Beyond the kinematic correction described before, the Drell-Yan component is categorized according to the number of jets, namely exactly two jets (2-jets category) and three or more jets (3-jets category), in order to account for NLO effects related to the modeling of extra jets [39]. Data-driven correction factors are derived after a proper categorization of the background processes, based on the flavor of the reconstructed jet. Those coming from the hadronization of b-quarks are classified as 'b', while those coming from charm, light quarks and gluons are classified as 'x'. The following scale factor (SF) nomenclature is then adopted:

- '**SF_Zbb**' rescales the Z+bb contribution in the 2-jet category only, dominated by the Z+bb process at leading order (i.e. without extra jets).
- '**SF_Zb(b)x**' rescales the Z+bb contribution in the 3-jet category, as well as the Z+b+x contribution in both the 2-jet and 3-jet categories. All three contributions are dominated by NLO effects in the Zbb final state.
- '**SF_Zxx**' rescales the Z+light-jets contribution in both the 2-jet and 3-jet categories.
- '**SF_tt**' rescales the $\text{t}\bar{\text{t}}$ contribution in both the 2-jet and 3-jet categories.

Scale factors for the background are left free to float in a two-dimensional fit to the shape of two observables, the product of the CSV discriminants of both selected jets and the invariant mass of the lepton pair from Z boson decay in the range $60 < M_{\ell\ell} < 120$ GeV. This fit is performed simultaneously in the four different categories (electrons, muons, exactly two jets, and more than two jets), after requiring the presence of at least a pair of same flavor opposite sign leptons and two b-tagged jets in the event. The first observable is sensitive to the contribution from non-b jets contamination, whereas the second variable is sensitive to the contamination of $\text{t}\bar{\text{t}}$ events. The variables used as input of the fit procedure are shown in Fig. 2. Given the negligible effect that a possible signal manifestation over the considered background fit range would bring, no specific control and signal regions have been defined for the derivation of the background scale factors. The SF_tt is found to be compatible with one (1.04 ± 0.03), while the fact that SF_Zxx (1.27 ± 0.10) and SF_Zb(b)x (1.27 ± 0.05) are significantly larger than one indicates a possible underestimation of the mis-tag fraction in the simulation. The SF_Zbb (1.16 ± 0.04) is found

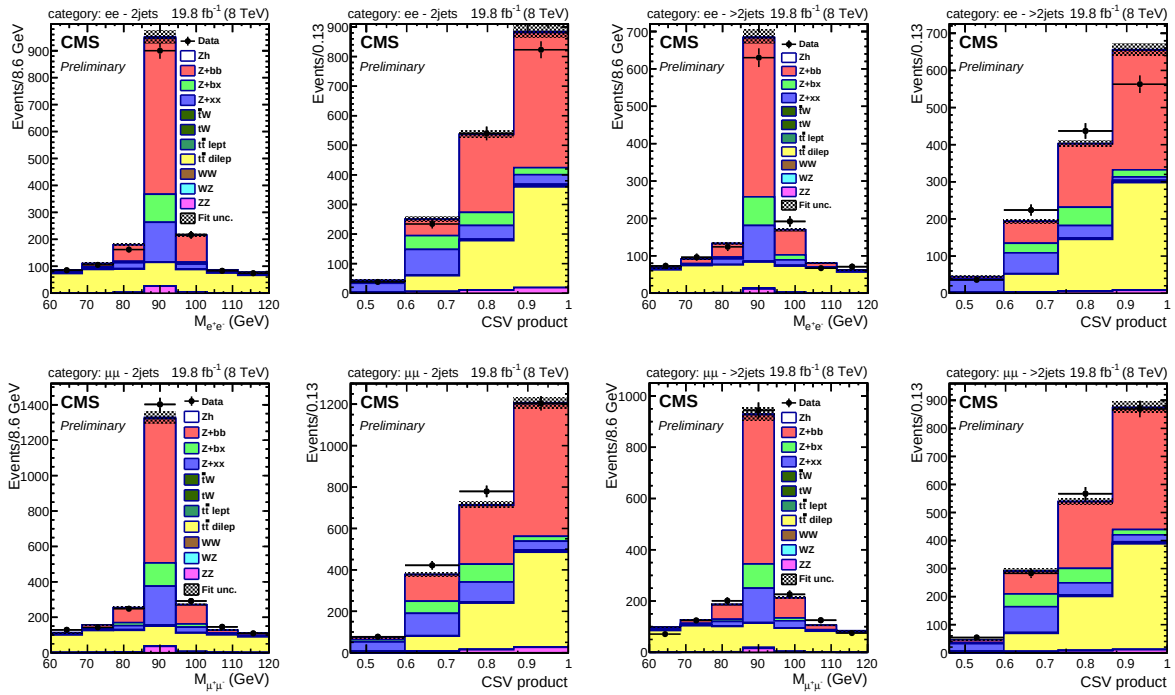

Figure 2: Input variables to the fit procedure for the estimation of background normalization factors. The first two columns show the results for the 2-jet exclusive bins, while the last two columns illustrate the results in the inclusive $>$ 2jet region. The first row refers to the electron channel, while the second row to the muon one. The backgrounds are shown normalized to the results of the fit. The uncertainty from the fit is shown as a hatched band.

to be compatible with the one measured in the SM Zh$\rightarrow \ell\ell$bb search at 8 TeV [40] and is also compatible with the Z+bb cross section measurement [39]. Results of the fit are obtained by considering events in the full M_{bb} and $M_{\ell\ell bb}$ range, although a check of their stability is performed in the two-dimensional M_{bb}-$M_{\ell\ell bb}$ sideband region outside a specific signal hypothesis mass bin and also by a signal injection for chosen values of M_A and M_H. The effect of the background normalization is shown on the two main observables of this search, M_{bb} and $M_{\ell\ell bb}$, in Fig. 3.

Selected events for the different backgrounds are computed after the background normalization and efficiency corrections, and compared with data. Table 1 reports the findings after the final selection step in the $\ell\ell$bb channel.

Table 1: Data and MC yields obtained after the final selection step in the $\ell\ell$bb channel, efficiency corrections and background normalization are applied to the simulated backgrounds. Statistical uncertainties are reported.

Zbb	Zbx	Zxx	tW	$t\bar{t}$	WZ	ZZ	WW	Zh	tot. MC	data
3039 $\pm$51	494$\pm$24	780$\pm$37	29$\pm$4	1270$\pm$8	12$\pm$1	113$\pm$1	0.3$\pm$0.2	21.5$\pm$0.1	5758$\pm$68	5776

5.2 The $\ell\ell\tau\tau$ channel

Methods based on data control samples and comparison with simulated events are used to estimate residual backgrounds after the selection described in Section 4. Normalizations and

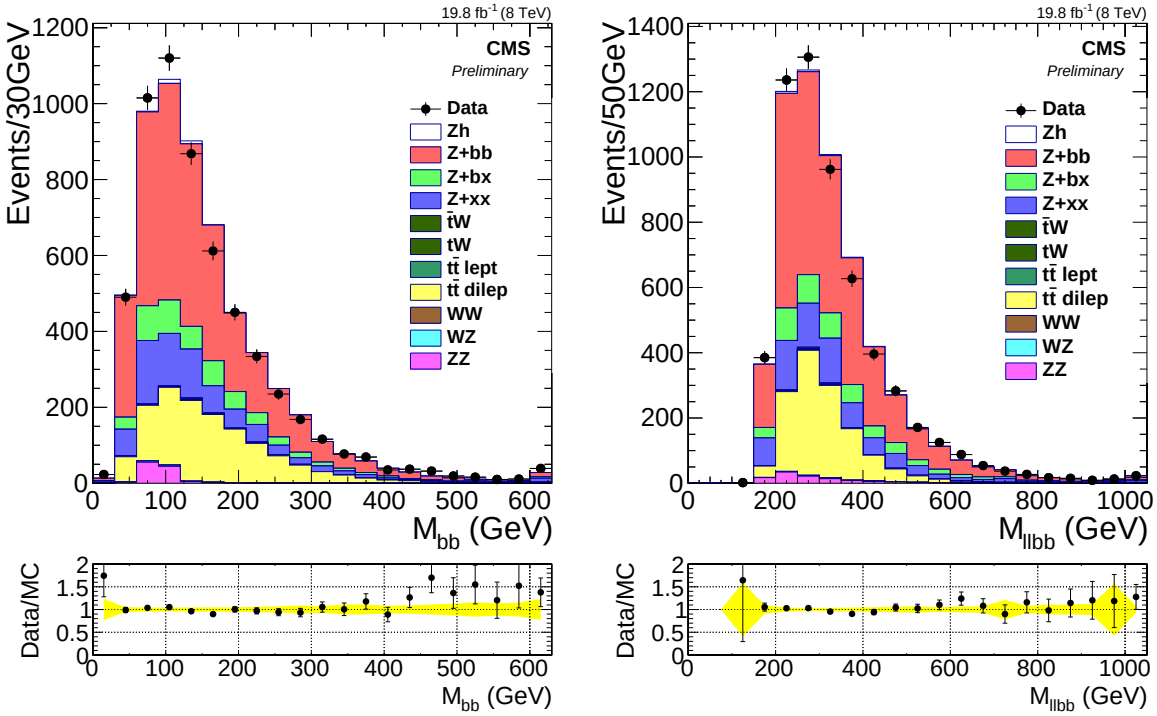

(a) (b)

Figure 3: The M_{bb} and $M_{\ell\ell bb}$ observables after the baseline selection, background normalization, and shape correction for NLO effects. Distributions combine the electron and muon channel of the H→ZA→ $\ell\ell$bb analysis. The last bin in both distributions contains the overflow. In the data/simulation ratio, the yellow band shows the statistical uncertainty in the simulated yield.

shapes of the main irreducible backgrounds (ZZ and SM Zh$\rightarrow \ell\ell\tau\tau$) are estimated from MC. Simulations are also used to estimate small contributions from the WWZ process, where one Z decays into a di-electron or di-muon pair and the W bosons decay leptonically, and fully leptonic $t\bar{t}$ Z decays, for which about 4% passes the selection in the $e\mu$ channel despite the b-jet veto.

Production of Z+jets and WZ+jets constitute the main sources of background with at least one misidentified lepton. Misidentified light leptons (μ or e) arise from the semileptonic decays of heavy flavor quarks, decays in flight, misidentified hadrons, and electrons from photon conversions, while quark or gluon jets can be wrongly reconstructed as hadronic taus. A data-driven approach is used to estimate this background.

The lepton misidentification probability is the probability that a genuine jet satisfying loose identification criteria, also passes the identification criteria required for the lepton candidate in the signal region ("tight" lepton). This probability is measured for each lepton flavor using a data sample where a Z candidate is selected, as explained in the Section 4, and an additional single lepton, electron, muon, or tau passes the loose identification requirements. By counting the number of these loose leptons that also pass the tight lepton identification criteria in bins of the p_T of the reconstructed jet closest to the loose lepton, the misidentification probability $f(p_T)$ is then obtained. The contribution of genuine leptons arising from the non-negligible WZ and ZZ($\rightarrow 4\ell$ and $\rightarrow 2\ell 2\tau$) production are subtracted.

Once the misidentification probabilities have been computed for each lepton flavor, three different control regions are defined where a Z candidate and two opposite-charge leptons are required. These control regions are defined as follows:

- **Control Region 00 (CR_{00}):** both leptons pass the loose identification criteria but not the tight ones;
- **Control Region 10 (CR_{10}):** one lepton passes the tight identification requirements, the other passes only the loose ones ("loose" lepton). In this control region the loose lepton is the sub-leading tau in the $\tau_h\tau_h$, the light lepton in the $\ell\tau_h$ and the electron in the $e\mu$ final state;
- **Control Region 01 (CR_{01}):** as in the control region CR_{10}, but in this case the loose lepton is the leading tau in the $\tau_h\tau_h$, the tau in the $\ell\tau_h$ and the muon in the $e\mu$ final state.

The estimate N_{fake} of the background with at least one misidentified lepton is given by the following expression:

$$N_{fake} = N_{10}\frac{f_1(p_T)}{1-f_1(p_T)} + N_{01}\frac{f_2(p_T)}{1-f_2(p_T)} - N_{00}\frac{f_1(p_T)f_2(p_T)}{(1-f_1(p_T))(1-f_2(p_T))}. \quad (2)$$

where N_{00}, N_{01}, and N_{10} denote the number of events in the CR_{00}, CR_{01}, and CR_{10} control regions, respectively, and $f_1(p_T)$ and $f_2(p_T)$ indicate the misidentification probabilities of the loose leptons in the control regions, as defined above. The expression in Eq. 2 takes into account both the background with two misidentified leptons (mostly from Z+jets) and that from only one misidentified lepton (primarily WZ+jets). The contamination of genuine leptons in the control regions from the SM Zh, WWZ, WZZ, ZZZ, $t\bar{t}$ Z and ZZ processes is estimated from simulation and is subtracted from N_{00}, N_{01} and N_{10}. In some cases the subtraction process gives negative values, which are treated with the Feldman-Cousins (FC) approach [41], i.e. considering zero as the best measurement estimate and the FC 68%CL upper limit on the measurement as statistical error. The reducible background yields, relative to the cut-and-count analysis and

corresponding to have no requirements on the L_T for all the channels, are reported in Table 2. These numbers are shown here for the sake of illustration only, as the reducible background estimate varies according to the L_T requirement found to be optimal for each channel and for each mass point. The same procedure described above has also been applied in every bin of the histograms used in the shape analysis. In this case, both same-sign and opposite-sign di-lepton pairs have been considered, whereas the normalization of the histograms is obtained from just the opposite-sign events.

Table 2: Final reducible background yields for all the eight final states obtained from data using Eq. 2. Statistical uncertainties are also reported.

channel	N_{fake} (Data)
$eee\mu$	0.15 ± 1.85
$eee\tau_h$	1.09 ± 1.21
$ee\mu\tau_h$	0.48 ± 1.82
$ee\tau_h\tau_h$	11.70 ± 2.58
$\mu\mu e\mu$	0.25 ± 1.90
$\mu\mu e\tau_h$	0.26 ± 0.93
$\mu\mu\mu\tau_h$	3.24 ± 1.18
$\mu\mu\tau_h\tau_h$	12.85 ± 2.84

A closure test, using the simulated samples of background with at least one misidentified lepton, has been performed. The data-driven method described above has been applied on these simulated samples and the resulting yield has been compared to the true yield in the signal region. The misidentification probabilities have also been obtained from the same simulated samples. This closure test allows to assess a systematic uncertainty of 40%, for all channels and all L_T thresholds, in the estimates of the reducible backgrounds obtained with this method.

6 Systematic uncertainties

Systematic uncertainties affecting the normalization and the shape of signal and background processes can bias the outcome of the search. Those affecting both decay channels considered in this search have been identified in:

- Luminosity: The uncertainty in the luminosity recorded by CMS is estimated to be 2.6% in the 2012 dataset [42].
- Effect from pile-up: The total inelastic cross section used to infer the pile-up in data from the instantaneous luminosity is varied by $\pm$5%, thereby affecting the pile-up distribution used in simulation. The variation observed on the background and signal yields, through its effect on the lepton isolation requirements, is found to be between 1-3%.
- Di-lepton selection and trigger efficiencies: The systematic uncertainty of the scale factor per lepton, applied to MC events to compensate for data/MC differences and hereby affecting the estimate of the final yields, is obtained with the tag-and-probe method [12], and is found to be of the order of 1% for muons and 2% for electrons. This uncertainty is expected to affect in the same way both signal and background processes estimated from simulation. Also, the double muon and double electron trigger uncertainties are evaluated to be of 1% by specific studies on the Z peak.
- Jet energy scale (JES) and resolution (JER): The uncertainty in the jet energy scale is taken from Ref. [43], and the values are varied up and down according to official recommendations. The effect on the background is estimated each time. The effect

on the signal is estimated to be 3–5% depending on the p_T and η of the jets. The uncertainty on the signal and background yields due to the imperfect knowledge of jet energy resolution in CMS detector is estimated to be of the order of 3%.

- B-tagging and mis-tag efficiency: the uncertainties affecting the b-tagging efficiencies are p_T-dependent and vary from 3% up to 12% (for $p_T < 30\,\text{GeV}$). These uncertainties are propagated to the b-tagging data/MC scale factors, as described in Ref. [44, 45], and found to be of the order of 5% for the background and 4-6% for the signal for the $\ell\ell$bb analysis, and of the order of 1% for the $\ell\ell\tau\tau$ one. The uncertainty on the mistagging rate, which enters the calculation of the event weight at second order, is found to have a negligible impact.

Specifically for the $\ell\ell$bb and $\ell\ell\tau\tau$ final states a set of additional systematics has been evaluated and their impact on the extracted upper limits has been quantified.

Table 3: Summary of systematic uncertainties on event yields of signal and background processes. The last column quotes whether the source of uncertainty is assigned as rate (normalization) uncertainty or as a shape (probability distribution function) uncertainty in the analysis.

	H→ZA→ $\ell\ell\tau\tau$		H→ZA→ $\ell\ell$bb	
Source	Uncertainty [%]	Type	Uncertainty [%]	Type
Luminosity	2.6	rate	2.6	rate
Pile-up effects	1-3	shape	1-3	rate
Lepton ID/Isolation/ES	2	rate	2	rate
Lepton trigger efficiency	1	rate	1	rate
Jet ES/resolution	3	shape	3	rate
Tau ID/Iso	6	rate	–	–
Tau ES	3	shape	–	–
Reducible bkg. estimate	40	rate	–	–
B-tagging and mis-tag efficiency	1	rate	5 (bkg.) 4-6 (signal)	rate
Bkg. normalization (ZZ)	11	rate	11	rate
Bkg. norm. (DY + jets and $t\bar{t}$)	–	–	< 8	rate
Bkg. norm. (tW,WW,WZ and Zh)	–	–	6-23	rate
Drell-Yan bkg. modelling	–	–	5–30	rate
Signal efficiency extrapolation	–	–	3-50	rate
Signal modelling (PDF, scale)	–	–	5-6	rate

Concerning the $\ell\ell$bb final state, the uncertainty on the background normalization scale factors derived in Section 5 for DY+jets and $t\bar{t}$ has been quantified using statistical uncertainty from the fit. Additionally, a systematic associated to the modeling of $M_{\ell\ell bb}$ spectrum after the reweighting performed in Section 5 has also been assigned and found to be 5–30% depending on the $M_{\ell\ell\text{bb}}$ mass considered. For the remaining backgrounds, uncertainty of 11% is assigned to the ZZ normalization [34] and 6-7% for the other diboson processes (WW, WZ) [35][36]. The size of the systematics has been derived using the uncertainty on the CMS measured cross-section for these SM processes. For the other minor background tW the uncertainty has been estimated to be around 23% from the measured cross section as well [37]. Uncertainty on the Zh process has been instead derived from the theoretical cross-section, and found to be of the order of 7% [38]. An uncertainty due to the extrapolation of the signal efficiency and acceptance for the different signal points in the M_H-M_A plane has also been evaluated, which is close to 3% in most of the phase space and goes up to 50% at the boundaries of the sensitivity region. Systematic un-

certainty on the signal has been evaluated by varying the set of Parton Distribution Functions (PDF) used and the factorization and renormalization scale. An effect of 5-6% is estimated on the entire mass range.

Regarding the $\ell\ell\tau\tau$ final state, the hadronic tau identification uncertainty has been determined to be 6% by CMS using the tag-and-probe type measurement. The hadronic tau energy scale uncertainty is within 3% and it affects the final mass shapes. The systematic uncertainties estimated on light leptons, taus and jets energy scales, have been propagated on the $E_{\mathrm{T}}^{\mathrm{miss}}$ and, therefore, on the mass shapes. The propagation on the $E_{\mathrm{T}}^{\mathrm{miss}}$ estimator has been done, firstly, summing light leptons, taus and jets energy contributions and, secondly, subtracting the corresponding object collection contributions, once the nominal energy scale (or resolution) have been varied by $\pm 1\sigma$ (for leptons, taus and jets). One of the main systematic uncertainty is the one related to the non-prompt background estimation. This uncertainty, estimated to be 40%, has been evaluated in the context of the closure test as it has been described in the Section 5. Additionally, as for the $\ell\ell$bb channel, 11% uncertainty is assigned to the ZZ normalization.

All the sources of systematic uncertainties are summarized in Table 3.

7 Results

Two moderate excesses are visible for the $\ell\ell$bb channel in the region around (M_{bb},$M_{\ell\ell\mathrm{bb}}$) = (93,286) GeV and (M_{bb}, $M_{\ell\ell\mathrm{bb}}$) = (575,662) GeV. They have respectively local significance of 2.6 and 2.85 σ, which become globally 1.6 and 1.9 σ once accounting for the Look Elsewhere Effect [46]. The CLs criterion [47, 48] is used to determine at 95% confidence level (CL) the upper limits on the signal cross section. The numerical values for the cross section upper limits and significance are derived with the asymptotic method reported in [49].

For the $\ell\ell$bb final state, results are obtained using a counting experiment approach. This approach has the advantage of being less model-dependent than a shape-based approach which relies on the shape of the expected signal. It can be then more easily reinterpreted in other theory models foreseeing the same final state. Results are reported in bins as a function of the M_{bb} and $M_{\ell\ell\mathrm{bb}}$ masses, ranging from 10 GeV up to 1 TeV for the M_{bb} and from 140 GeV up to 1 TeV for the $M_{\ell\ell\mathrm{bb}}$. In order to define the proper granularity of the binning, a study has been performed by using DELPHES simulation of few signal benchmark points and evaluating the width of the M_{bb} and $M_{\ell\ell\mathrm{bb}}$ peaks in the considered mass range. The average reconstructed width for M_{bb} and $M_{\ell\ell\mathrm{bb}}$ is found to be of the order of 15% of the mass considered (defined as σ). The amplitude of the bin has been therefore chosen to be $\pm 1.5\sigma$ around each considered mass point.

In order to interpret the results in terms of upper limits on the production cross section for a specific 2HDM type, the signal efficiencies, defined as the fraction of events reconstructed in the detector acceptance, are calculated using 13 representative signal points in the 2D plane. A realistic prediction of the efficiencies for the rest of the mass space is instead derived from DELPHES simulation of the signal mass points and combined with proper interpolation with the existing 13 reference points. A signal efficiency map, based on the convolution of a full and fast simulation, is shown in Fig. 4.

The left (right) plot of Fig. 5 shows instead the expected (observed) upper exclusion limits in terms of cross section times branching ratio for the $\ell\ell$bb final state. The achieved sensitivity allows to exclude at 95%CL values of cross section times branching ratio of the order of 10 fb for a large fraction of the 2D mass plane. The final observed exclusion limit ranges from few fb

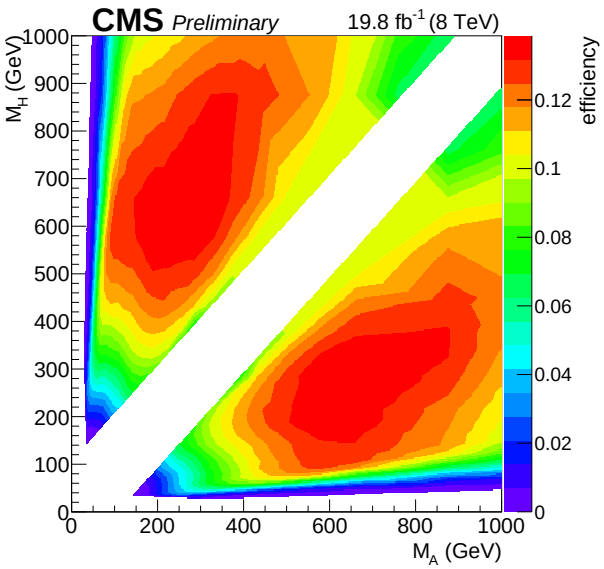

Figure 4: Efficiency map obtained from an hybrid generation of signal mass points (CMSSW simulation interpolated with DELPHES.) for the $\ell\ell$bb final state.

for M_H close to 1 TeV to 100 fb for M_H <300 GeV. The validity of these results can be extended to models containing both A and H with a natural width smaller than 15% of their masses.

The expected (observed) upper limits on the signal cross section modifier μ are shown in the right (left) plot of Fig. 6, assuming the benchmark models described in Section 3. This search is not able to exclude the high-mass region ($M_A > 300$ GeV) due to the drop in the signal cross section when the $t\bar{t}$ channel opens ($M_A > 2M_{top}$). Furthermore, it can be noticed that, in the region where boosted topologies manifest ($M_H \sim 10 \cdot M_A$), the sensitivity is lower compared to the rest of the plane, mostly due to the inefficiency in the reconstruction of signal decay products in such regime. Still a significant portion of the phase space is excluded in the range [20-250] GeV for M_{bb} and [200-650] GeV for $M_{\ell\ell bb}$ both considering the decay H→ZA and A→ZH (solid contour on right plot of Fig. 6). The region where $M_{H/A} < M_{A/H} + M_Z$ is kinematically forbidden.

The limits on the cross section times branching ratio can also be visualized as a limit on $\tan\beta$ and $\cos(\beta - \alpha)$ for a given pair of M_A and M_H. This is illustrated in Fig. 7 where the limits on these two parameters is shown for the case $M_H = 350$ GeV and $M_A = 150$ GeV. The dashed region in the center of this plot shows the parameter space which is currently excluded for the pair of masses chosen. The region around $\cos(\beta - \alpha) \approx 0$ is of particular interest as it is generally difficult to probe with other analyses. For this case, the region where $\tan\beta$ lies between 0.2 and 2 is excluded.

In the context of the $\ell\ell\tau\tau$ analysis, both a cut-and-count and a shape-based search, which uses the $M_{\tau\tau}$ distribution, have been performed.

The cut-and-count approach, which uses only the number of signal and background events passing a selection depending on $M_{\ell\ell}$ and $M_{\ell\ell\tau\tau}$, is less model dependent and less affected by systematic uncertainties than the shape-based approach, which is instead more sensitive to the benchmark signal model explored in this search. The shape-based search also yields expected upper limits on the signal cross section times branching ratios that are about 20-30% lower than those obtained with the cut-and-count approach in most of the M_H-M_A plane. The expected

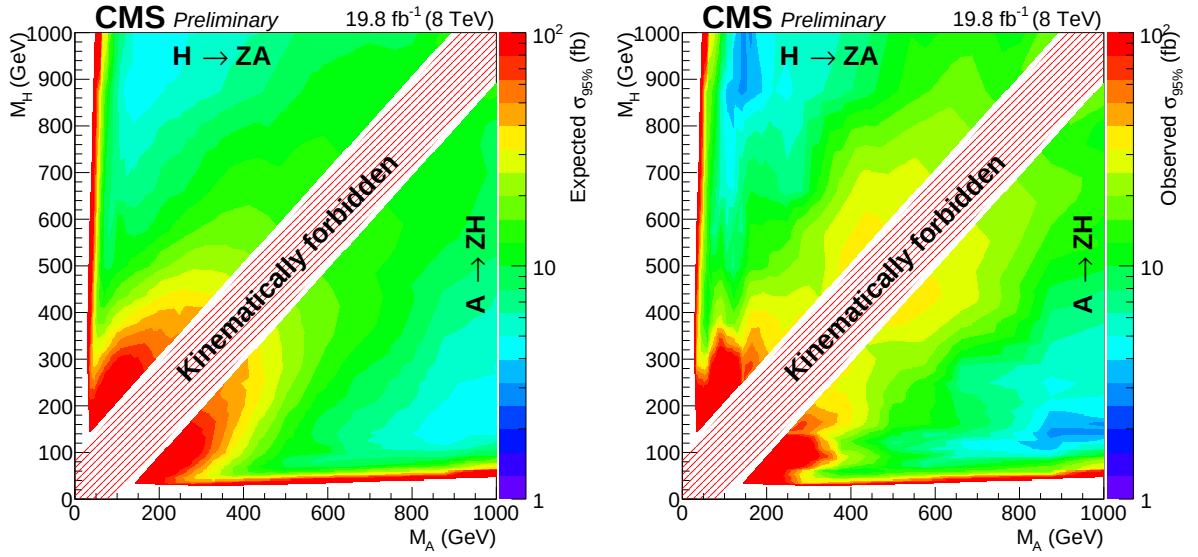

(a) (b)

Figure 5: Expected (a) and observed (b) upper limits on $\sigma_{H/A\to ZA/H\to\ell\ell bb}$ as a function of M_A and M_H after the convolution with efficiency and acceptance map for the $\ell\ell$bb final state.

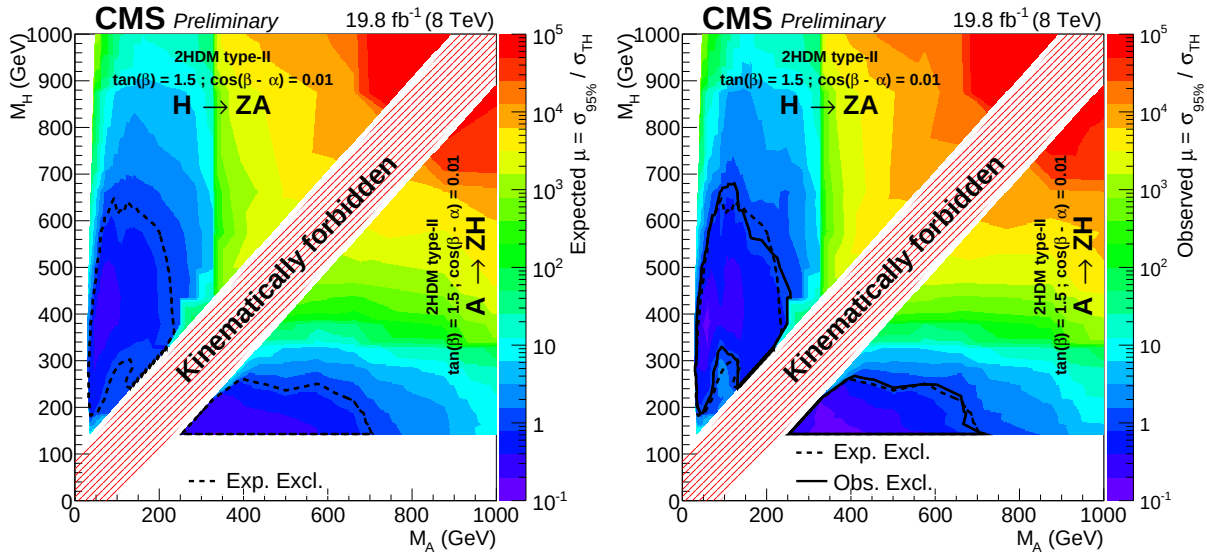

(a) (b)

Figure 6: Expected (a) and observed (b) limits on the signal strength $\mu = \sigma_{exp}/\sigma_{TH}$ for the 2HDM benchmark considered for $\ell\ell$bb final state. The cross section is normalized to the NNLO `SusHi` predictions. The dashed contour in both plots show the region which is expected to be excluded. In the right plot the solid contour shows the region which is excluded by data observation.

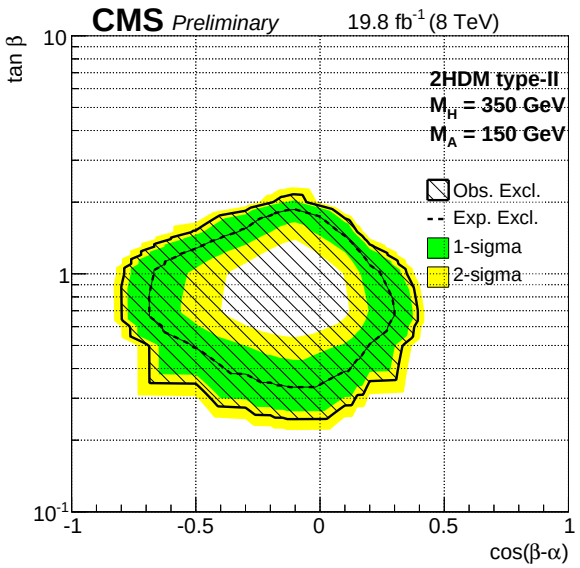

Figure 7: Expected (dashed line) and observed (solid line) 95%CL limits on $\cos(\beta-\alpha)$ and $\tan(\beta)$ for the 2HDM benchmark considered for $\ell\ell$bb final state and for $M_H = 350\,\text{GeV}$ and $M_A = 150\,\text{GeV}$. The green and yellow bands correspond respectively to the 1 and 2 standard deviations from the expected limits. The dashed region corresponds to the zone that is excluded by this search.

Table 4: Expected number of signal and background events compared to the number of observed events in data for an integrated luminosity of 19.8 fb $^{-1}$ at $\sqrt{s}$ =8 TeV and after having applied the final signal selection. The signal M_H =200 GeV-M_A =50 GeV is normalized to $\sigma\times$BR=1 fb. The yields correspond to L_T >20 GeV for $e\mu$, $\mu\tau_h$ and $\tau_h\tau_h$ and L_T >40 GeV for $e\tau_h$. The statistical uncertainties are reported for all the signal and background processes, while only systematic uncertainties related to the reducible background estimated from data are shown. All the other systematic uncertainties affecting the rate, and listed in Table 3, are included in the final limit computation.

	Channels			
	$e\tau_h$	$e\mu$	$\tau_h\tau_h$	$\mu\tau_h$
	$\mathbf{H}(200)\rightarrow\mathbf{ZA}(50)$			
SM Zh	0.266 ± 0.012	0.224 ± 0.011	0.665 ± 0.019	0.616 ± 0.018
WZZ	0.0158 ± 0.0054	0.0215 ± 0.0064	0.0210 ± 0.0061	0.0206 ± 0.0062
ZZZ	0.0032 ± 0.0012	0.0037 ± 0.0013	0.0095 ± 0.0020	0.0067 ± 0.0017
WWZ	0.136 ± 0.028	0.460 ± 0.053	0.025 ± 0.012	0.187 ± 0.033
$t\bar{t}$ Z	0.022 ± 0.022	0.217 ± 0.067	0.021 ± 0.021	0.062 ± 0.036
ZZ→4l	0.309 ± 0.020	0.0605 ± 0.0089	0.344 ± 0.021	0.279 ± 0.019
ZZ→2l2τ	3.891 ± 0.071	4.344 ± 0.075	11.40 ± 0.12	11.46 ± 0.12
Fakes	$0.9 \pm 1.3 \pm 0.3$	$0.4 \pm 2.7 \pm 0.1$	$24.5 \pm 3.8 \pm 6.9$	$3.7 \pm 2.2 \pm 1.3$
Total bkg.	5.5 ± 1.3	5.7 ± 2.7	37.0 ± 3.8	16.3 ± 2.2
Signal	0.0326 ± 0.0038	0.058 ± 0.0050	0.1100 ± 0.0069	0.1379 ± 0.0077
Data	5	7	42	8

number of signal and background events obtained at the end of the selection compared to those observed in data are summarized in Table 4 for only one mass pair selection for sake of illustration: M_H=200 GeV-M_A=50 GeV. For both analyses, the number of events observed is found compatible with the expected SM background.

In the shape-based analysis, non-constant mass bin widths have been adopted in order to account for the $M_{\tau\tau}$ resolution. The $M_{\tau\tau}$ shapes corresponding to the same reference selection

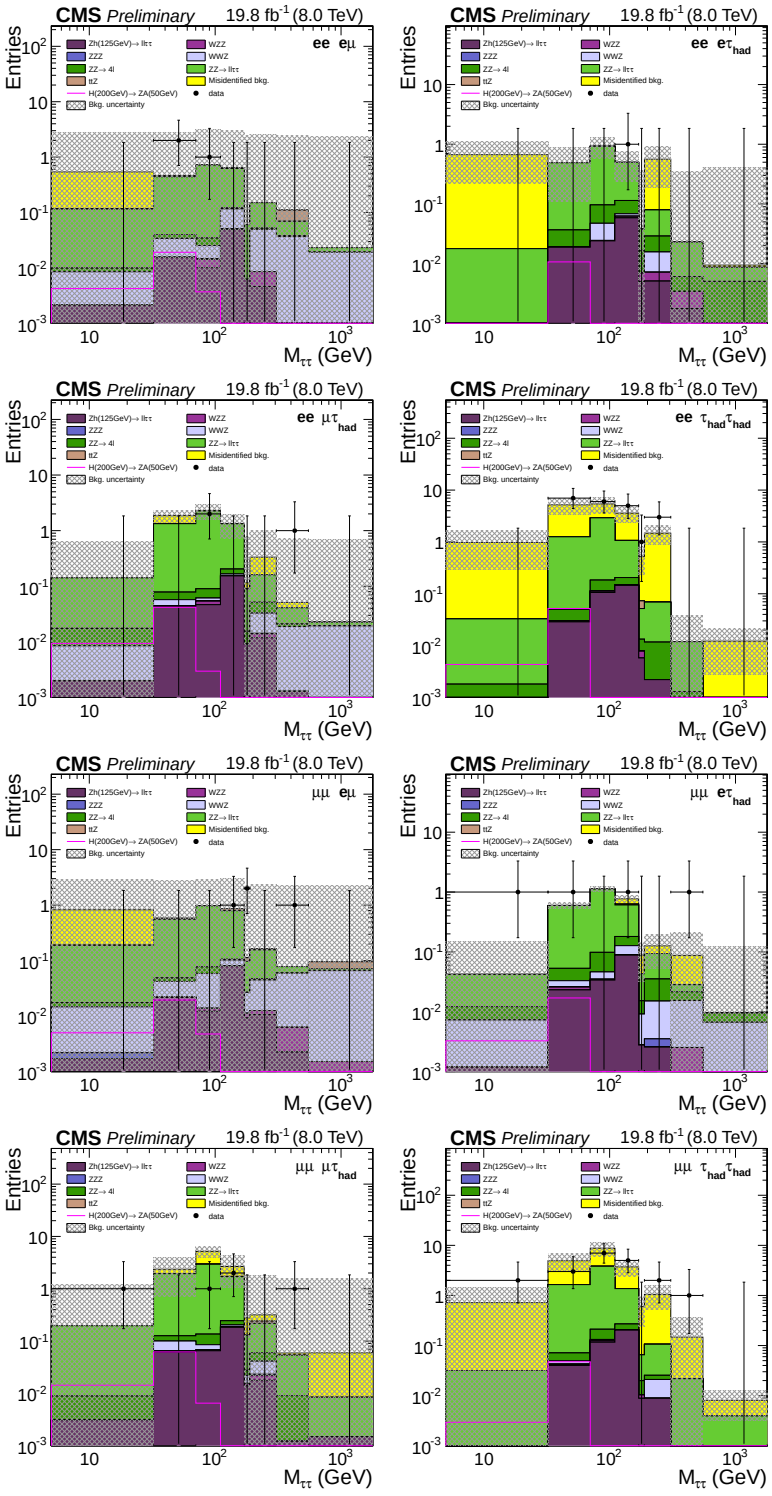

Figure 8: $M_{\tau\tau}$ distributions for the signal M_H=200 GeV and M_A=50 GeV. The distributions correspond to L_T >20 GeV for $e\mu$, $\mu\tau_h$ and L_T >40 GeV for $e\tau_h$ and $\tau_h\tau_h$. Statistical uncertainty bars have extrema computed using the Garwood procedure [50]. The signal is normalized to $\sigma\times$BR=1 fb.

are reported in Fig. 8.

Fig. 9 shows the limit on the $\sigma \times BR$ in the M_H-M_A plane: in particular, Fig. 9a and 9b show

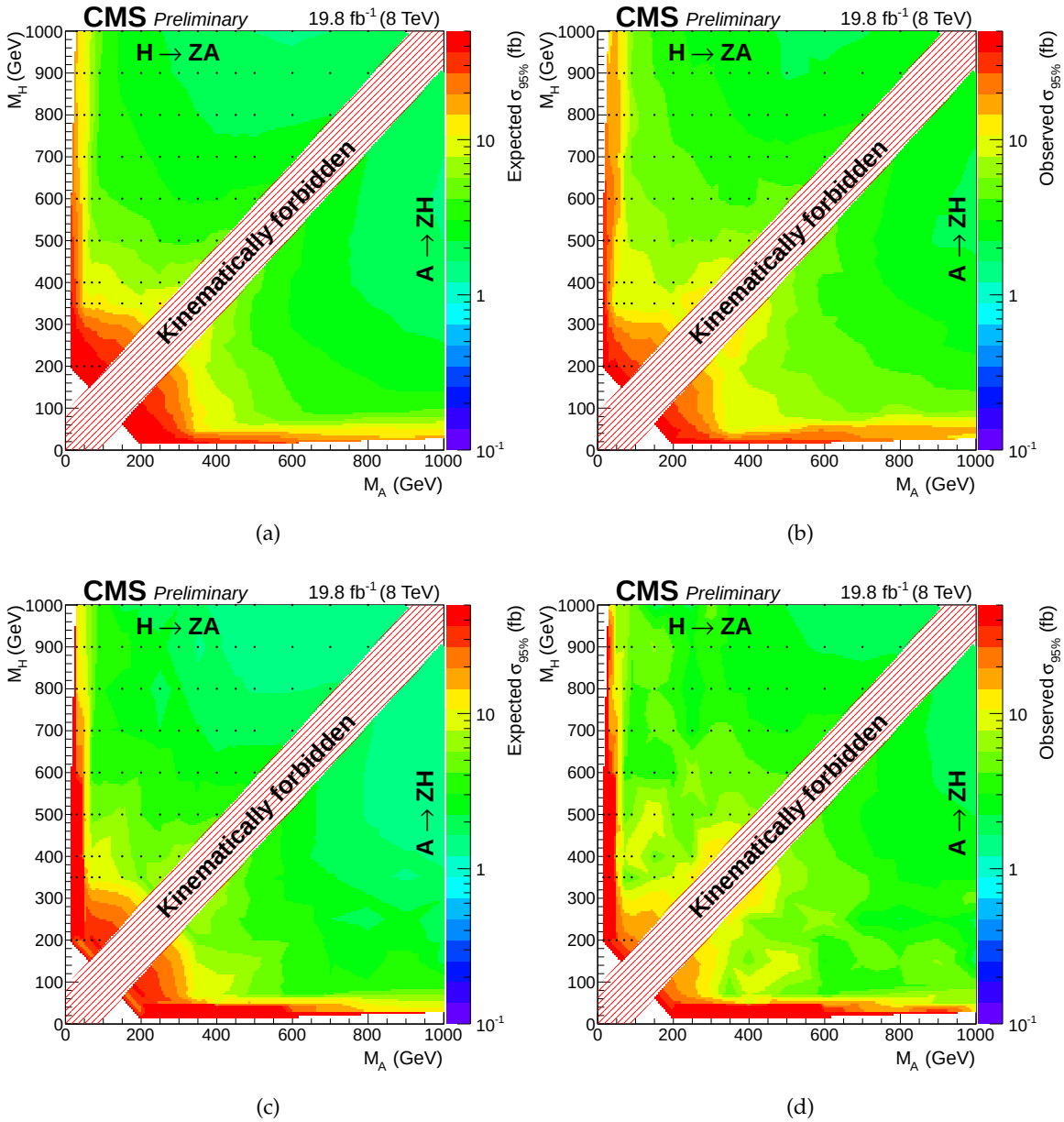

Figure 9: Limits on $\sigma_{H/A\to ZA/H\to\ell\ell\tau\tau}$ as a function of M_A and M_H for the $\ell\ell\tau\tau$ final state. Expected and observed limits for the cut-and-count analysis are reported in (a) and (b), while the corresponding results for the shape-based analysis are shown in (c) and (d), respectively. On top of the plots, black dots, referring to the full simulated signal samples, are shown.

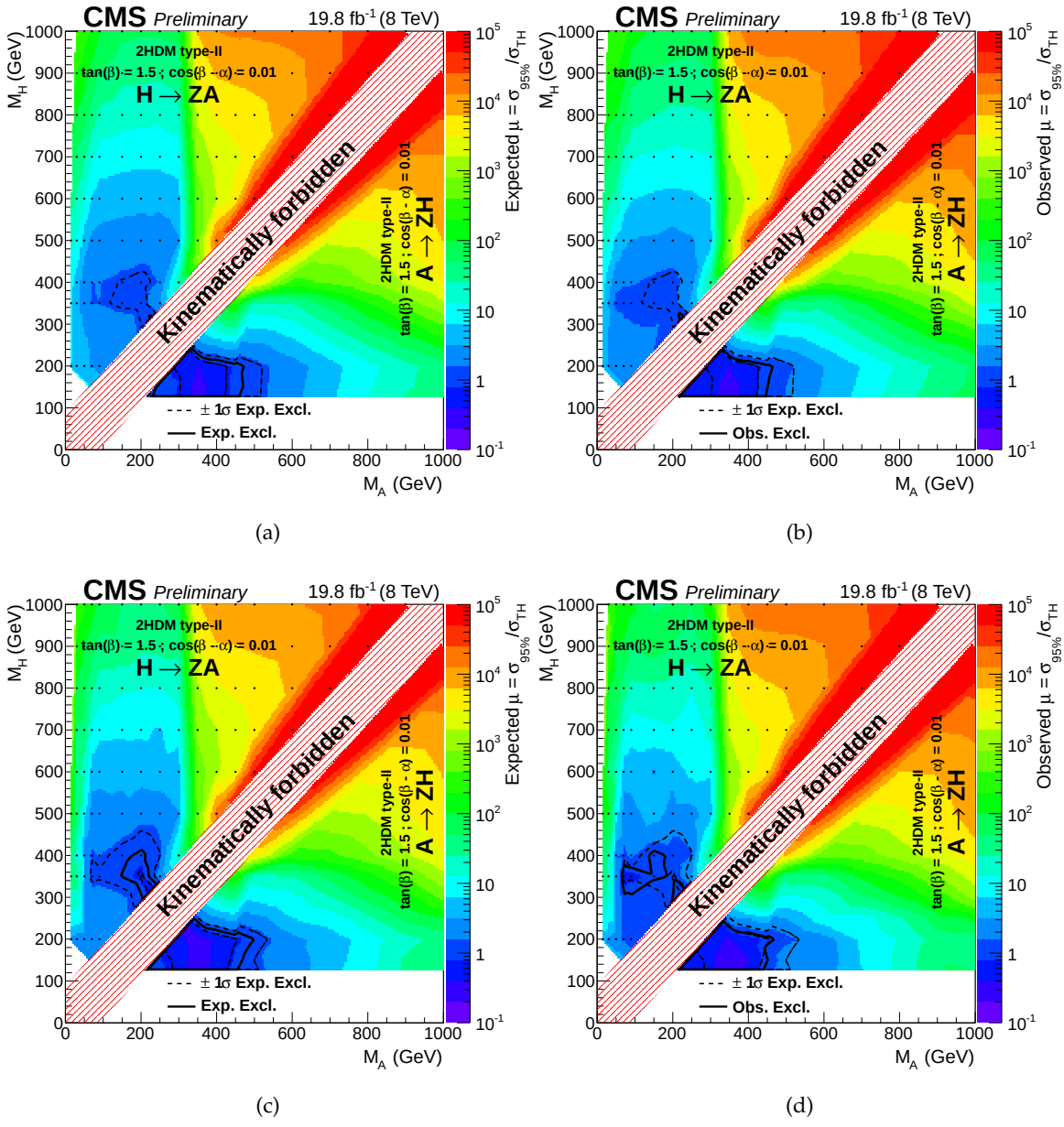

Figure 10: Limits on $\mu = \sigma_{95\%}/\sigma_{TH}$ for the $\ell\ell\tau\tau$ final state as function of the A and H boson masses. Expected and observed limits for the cut-and-count analysis are reported in (a) and (b), while the corresponding results for the shape-based analysis are shown in (c) and (d), respectively. The black dots refer to the full simulated signal samples. $\pm 1\sigma$ expected exclusion contours are drawn (dashed lines), together with the actual excluded regions delimited with solid lines.

the expected and observed limits, respectively, for the cut-and-count analysis, while Fig. 9c and 9d show the corresponding results for the shape-based analysis. Black dots indicate the signal samples that have been fully simulated. The limits at points in the rest of the plane have been obtained by interpolation. The limits in the lower-right triangle, which corresponds to the process A→ZH, have been obtained by simply mirroring the results obtained in the higher-left triangle because signal selection efficiency for H→ZA and A→ZH is the same provided that the masses of the heavy and light bosons in the two processes are the same. The kinematically forbidden region is the one where $M_{H/A} < M_{A/H} + M_Z$ and is also reported in Fig. 10. As can be seen from the plot, a cross section of about 5 fb is excluded in the majority of the M_H-M_A plane (500$<$ $M_{H/A}$ $<$1000 GeV and 90$<$ $M_{A/H}$ $<$400 GeV) for both cut-and-count and shape-based analysis.

Limits on the signal strength $\mu = \sigma/\sigma_{TH}$, where the σ_{TH} is the NNLO theoretical prediction for the cross section as given by `SusHi`, are shown in Fig. 10. Fig. 10a and 10b show the expected and observed limits, respectively, for the cut-and-count analysis, while Fig. 10c and 10d show the corresponding results for the shape-based analysis. The 95%CL expected excluded regions with 68% of probability, which are the same for both expected and observed limits, are delimited by dashed lines.

The excluded regions, different between expected and observed limits, are instead delimited by solid black lines. In the benchmark signal model scenario, the region where $M_{H/A} < M_h$ is forbidden. This kind of white regions are not reported in Fig. 9, instead, which shows model-independent results that may be reinterpreted in any other theoretical context.

As for the $\ell\ell$bb final state, the visualization of the limits on the cross section times branching ratio in the $\tan\beta$ and $\cos(\beta-\alpha)$ parameter space is provided in Fig. 11, for both cut-and-count (left) and shape-based analysis (right). The mass pair considered is the same as for the $\ell\ell$bb final state. Looking at the dashed region, which is the one currently excluded for the pair of masses chosen, it can be seen that, for $\cos(\beta-\alpha) \approx 0$, values of $\tan\beta$ roughly between 0.5 and 1.5 are excluded in the context of the shape-based analysis, while a smaller interval [0.5,1.3] is excluded for the cut-and-count one.

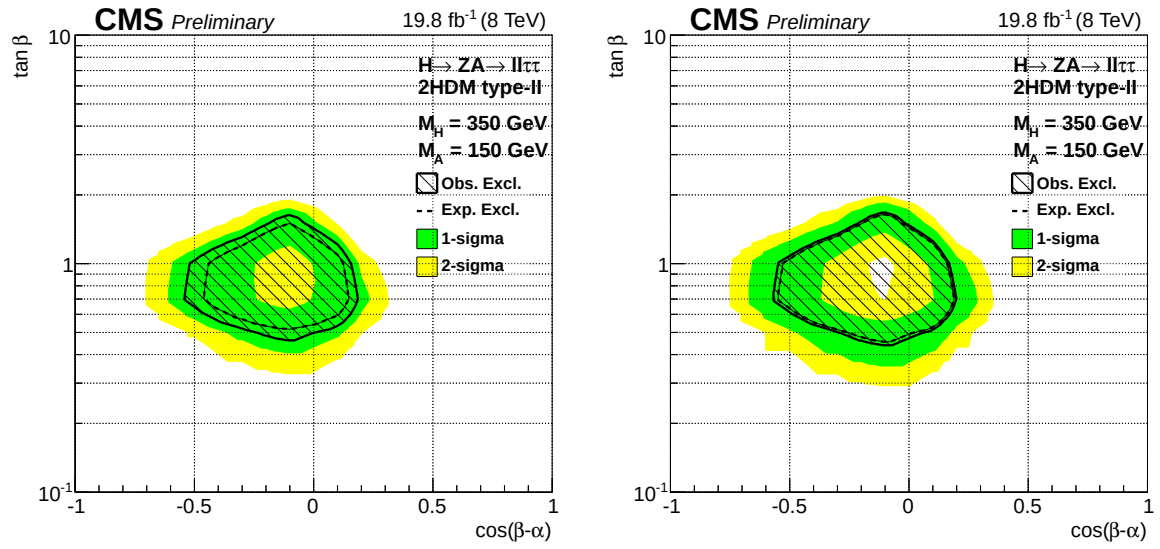

(a) (b)

Figure 11: Expected (dashed line) and observed (solid line) 95%CL limits, in the context of the cut-and-count (a) and the shape-based analysis (b), on $\cos(\beta - \alpha)$ and $\tan(\beta)$ for the 2HDM benchmark considered for $\ell\ell\tau\tau$ final state and for $M_H = 350\,\text{GeV}$ and $M_A = 150\,\text{GeV}$. The green and yellow bands correspond respectively to the 1 and 2 standard deviations from the expected limits. The dashed region corresponds to the zone that is currently excluded.

8 Summary

A search has been performed for a heavy resonance decaying to a Z boson and a light resonance, giving rise to $\ell\ell$bb and $\ell\ell\tau\tau$ final states, where the light resonance decays to either a pair of bottom quarks or a pair of tau leptons and the Z boson decays to two electrons or two muons. No significant deviations from the expectations of the standard model are observed and upper limits on the cross section times branching fraction are set using a dataset corresponding to an integrated luminosity of 19.8 fb $^{-1}$ at $\sqrt{8}$ TeV of proton–proton collisions. The search excludes cross sections times branching fractions as low as 1 fb (5 fb) for the $\ell\ell\tau\tau$ ($\ell\ell$bb) final state, depending on the light and heavy resonance masses.

Limits have also been set on type II 2HDM models, which predict the process H/A$\rightarrow$ ZA/H, where H and A are CP-even and CP-odd scalar bosons, respectively. In particular the model considered corresponds to the parameters $\cos(\beta-\alpha)$= 0.01 and $\tan\beta$ = 1.5.

Concerning the $\ell\ell$bb final state, it has been shown that the considered 2HDM benchmark scenario is excluded in the range [20,250] GeV for $M_{A/H}$ and [200,650] GeV for $M_{H/A}$ for the processes H/A$\rightarrow$ZA/H. The search in the $\ell\ell\tau\tau$ final state excludes masses of the H boson in the ranges [125,250] and [300,400] GeV and for the A boson in the range [125,400] GeV.

Limits have been also derived as a function of $\tan\beta$ and $\cos(\beta-\alpha)$ parameters. It has been shown that, for some choices of M_H-M_A values, some regions in the parameter space $\tan\beta$-$\cos(\beta-\alpha)$ can be excluded. In particular, for $M_H = 350$ GeV and $M_A = 150$ GeV, for $\cos(\beta-\alpha) \approx 0$ a $\tan\beta$ range roughly between 0.2 and 2 can be excluded for the $\ell\ell$bb channel. Considering the same mass point, for the $\ell\ell\tau\tau$ final state, both in the context of the cut-and-count and the shape-based analysis and for $\cos(\beta-\alpha) \approx 0$, the interval $0.5 < \tan\beta \leq 1.5$ is excluded.

References

[1] CMS Collaboration, "Observation of a new boson at a mass of 125 GeV with the CMS experiment at the LHC", *Phys. Lett.* **B716** (2012) 30–61, doi:10.1016/j.physletb.2012.08.021, arXiv:1207.7235.

[2] ATLAS Collaboration, "Observation of a new particle in the search for the Standard Model Higgs boson with the ATLAS detector at the LHC", *Phys. Lett.* **B716** (2012) 1–29, doi:10.1016/j.physletb.2012.08.020, arXiv:1207.7214.

[3] CMS Collaboration, "Evidence for the direct decay of the 125 GeV Higgs boson to fermions", *Nature Phys.* **10** (2014) 557–560, doi:10.1038/nphys3005, arXiv:1401.6527.

[4] G. Branco et al., "Theory and phenomenology of two-Higgs-doublet models", *Phys. Rept.* **516** (2012) 1–102, doi:10.1016/j.physrep.2012.02.002, arXiv:1106.0034.

[5] G. Dorsch, S. Huber, K. Mimasu, and J. No, "Echoes of the Electroweak Phase Transition: Discovering a second Higgs doublet through $A_0 \to ZH_0$", *Phys. Rev. Lett.* **113** (2014), no. 21, 211802, doi:10.1103/PhysRevLett.113.211802, arXiv:1405.5537.

[6] S. P. Martin, "A Supersymmetry primer", *Adv.Ser.Direct.High Energy Phys.* **21** (2010) 1–153, doi:10.1142/9789814307505_0001, arXiv:hep-ph/9709356.

[7] J. E. Kim, "Light Pseudoscalars, Particle Physics and Cosmology", *Phys. Rept.* **150** (1987) 1–177, doi:10.1016/0370-1573(87)90017-2.

[8] A. Broggio et al., "Limiting two-Higgs-doublet models", *JHEP* **1411** (2014) 058, doi:10.1007/JHEP11(2014)058, arXiv:1409.3199.

[9] F. Jegerlehner and A. Nyffeler, "The Muon g-2", *Phys. Rept.* **477** (2009) 1–110, doi:10.1016/j.physrep.2009.04.003, arXiv:0902.3360.

[10] CMS Collaboration, "The CMS experiment at the CERN LHC", *JINST* **3** (2008) S08004, doi:10.1088/1748-0221/3/08/S08004.

[11] CMS Collaboration, "Performance of electron reconstruction and selection with the CMS detector in proton-proton collisions at $\sqrt{s} = 8$ TeV", arXiv:1502.02701.

[12] CMS Collaboration, "Performance of CMS muon reconstruction in pp collision events at $\sqrt{s} = 7$ TeV", *JINST* **7** (2012) P10002, doi:10.1088/1748-0221/7/10/P10002, arXiv:1206.4071.

[13] J. Alwall et al., "MadGraph 5 : Going Beyond", *JHEP* **06** (2011) 128, doi:10.1007/JHEP06(2011)128, arXiv:1106.0522.

[14] T. Sjöstrand, S. Mrenna, and P. Skands, "PYTHIA 6.4 physics and manual", *JHEP* **05** (2006) 026, doi:10.1088/1126-6708/2006/05/026, arXiv:hep-ph/0603175.

[15] S. Alioli, P. Nason, C. Oleari, and E. Re, "A general framework for implementing NLO calculations in shower Monte Carlo programs: the POWHEG BOX", *JHEP* **06** (2010) 043, doi:10.1007/JHEP06(2010)043, arXiv:1002.2581.

[16] GEANT4 Collaboration, "GEANT4: A Simulation toolkit", *Nucl. Instrum. Meth.* **A506** (2003) 250–303, doi:10.1016/S0168-9002(03)01368-8.

[17] CMS Collaboration, "Measurement of the Inclusive W and Z Production Cross Sections in pp Collisions at $\sqrt{s}$ = 7 TeV", *JHEP* **10** (2011) 132, doi:arXiv:1107.4789.

[18] S. Jadach, Z. Was, R. Decker, and J. H. Kuhn, "The tau decay library TAUOLA: Version 2.4", *Comput. Phys. Commun.* **76** (1993) 361–380, doi:10.1016/0010-4655(93)90061-G.

[19] R. Harlander et al., "SusHi: A program for the calculation of Higgs production in gluon fusion and bottom-quark annihilation in the Standard Model and the MSSM", *Comp. Phys. Commun.* **184** (2013) 1605–1617, doi:10.1016/j.cpc.2013.02.006.

[20] J. de Favereau et al., "DELPHES 3, A modular framework for fast simulation of a generic collider experiment", *JHEP* **02** (2014) 057, doi:10.1007/JHEP02(2014)057.

[21] W. Adam et al., "PAT: The CMS Physics Analysis Toolkit", *J. Phys. Conf. Ser.* **219** (2010) 32017, doi:doi:10.1088/1742-6596/219/3/032017.

[22] CMS Collaboration, "Commissioning of the Particle-Flow reconstruction in Minimum-Bias and Jet Events from pp Collisions at 7 TeV", *CMS Physics Analysis Summary* **CMS-PAS-PFT-10-002** (2010).

[23] CMS Collaboration, "Particle–Flow Event Reconstruction in CMS and Performance for Jets, Taus and Missing E_T", *CMS Physics Analysis Summary* **CMS-PAS-PFT-09-001** (2009).

[24] CMS Collaboration, "Particle-flow commissioning with muons and electrons from J/Ψ and W events at 7 TeV", *CMS Physics Analysis Summary* **CMS-PAS-PFT-10-003** (2010).

[25] E. Chabanat and N. . Estre, "Deterministic Annealing for Vertex Finding at CMS", *Computing in High Energy Physics and Nuclear Physics* (2004) 287, doi:10.5170/CERN-2005-002.287.

[26] CMS Collaboration, "Performance of CMS muon reconstruction in pp collision events at $\sqrt{s} = 7$ TeV", (2012). arXiv:1206.4071. Submitted to *J. Inst.*

[27] CMS Collaboration, "Electron reconstruction and identification at $\sqrt{s} = 7$ TeV", technical report, 2010.

[28] CMS Collaboration, "Performance of tau–lepton reconstruction and identification in CMS", *JINST* **7** (2012) P01001, doi:10.1088/1748-0221/7/01/P01001, arXiv:1109.6034.

[29] M. Cacciari, G. P. Salam, and G. Soyez, "The anti-k_t jet clustering algorithm", *JHEP* **04** (2008) 063, doi:10.1088/1126-6708/2008/04/063, arXiv:0802.1189.

[30] CMS Collaboration, "Identification of b-quark jets with the CMS experiment", *JINST* **8** (2013) P04013, doi:10.1088/1748-0221/8/04/P04013, arXiv:1211.4462.

[31] Particle Data Group, J. Beringer et al., "Review of Particle Physics", *Phys. Rev. D* **86** (2012) 010001, doi:10.1103/PhysRevD.86.010001.

[32] L. Bianchini, J. Conway, E. Klose Friis, and C. Veelken, "Reconstruction of the Higgs mass $H/rightarrow/tau/tau$ Events by Dynamical Likelihood techniques", *Journal of Physics* **503** (2014) doi:10.1088/1742-6596/513/2/022035.

[33] CMS Collaboration, "2012 ECAL detector performance plots", *CMS-DP* **CMS-DP-2013-007** (2013).

[34] CMS Collaboration, "Measurement of the pp $\to$ ZZ production cross section and constraints on anomalous triple gauge couplings in four-lepton final states at $\sqrt{s}$ = 8 TeV", *Phys. Lett. B* **740** (Jun, 2014) 250. 31 p, doi:http://dx.doi.org/10.1016/j.physletb.2014.11.059.

[35] CMS Collaboration, "Measurement of the WW cross section in pp collisions at $\sqrt{s}$= 8 TeV and limits on anomalous gauge couplings", *CMS-PAS* **SMP-14-016** (2014).

[36] CMS Collaboration, "WZ inclusive and differential cross section and limits on anomalous gauge couplings", *CMS-PAS* **SMP-14-014** (2014).

[37] CMS Collaboration, "Observation of the associated production of a single top quark and a W boson in pp collisions at $\sqrt{s}$=8 TeV", *CMS-PAS* **TOP-12-040** (2012).

[38] CMS Collaboration, "Search for the standard model Higgs boson produced in association with a *W* or a *Z* boson and decaying to bottom quarks", *Phys. Rev. D* **89** (Jan, 2014) 012003, doi:10.1103/PhysRevD.89.012003.

[39] CMS Collaboration, "Measurement of the production cross sections for a Z boson and one or more b jets in pp collisions at $\sqrt{s} = 7$ TeV", *JHEP* **06** (2014) 120, doi:10.1007/JHEP06(2014)120.

[40] CMS Collaboration, "Search for the standard model Higgs boson produced in association with a W or a Z boson and decaying to bottom quarks", *Phys. Rev. D* **89** (2014) 12003, doi:10.1103/PhysRevD.89.012003.

[41] G. J. Feldman and R. D. Cousins, "A Unified approach to the classical statistical analysis of small signals", *Phys. Rev.* **D57** (1998) 3873–3889, doi:10.1103/PhysRevD.57.3873, arXiv:physics/9711021.

[42] CMS Collaboration, "CMS Luminosity Based on Pixel Cluster Counting - Summer 2013 Update", *CMS Physics Analysis Summary* **CMS-PAS-LUM-13-001** (2013).

[43] N. Saoulidou and M. Zielinski, "Jet Energy Resolution Measurement", twiki page, 2011.

[44] CMS Collaboration, "Performance of the b-jet identification in CMS", *CMS Physics Analysis Summary* **CMS-PAS-BTV-11-001** (2011).

[45] CMS Collaboration, "b-Jet Identification in the CMS experiment", *CMS Physics Analysis Summary* **CMS-PAS-BTV-11-004** (2011).

[46] E. Gross and O. Vitells, "Trial factors for the look elsewhere effect in high energy physics", *European Physical Journal* **C 70** (2010) 525–530, doi:doi:10.1140/epjc/s10052-010-1470-8.

[47] A. L. Read, "Modified frequentist analysis of search results (the CLs method)", CERN Report CERN-OPEN-2000-005, 2000.

[48] T. Junk, "Confidence level computation for combining searches with small statistics", *Nucl. Instrum. Meth.* **A434** (1999) 435–443, doi:10.1016/S0168-9002(99)00498-2, arXiv:hep-ex/9902006.

[49] G. Cowan, K. Cranmer, E. Gross, and O. Vitells, "Asymptotic formulae for likelihood-based tests of new physics", *Eur. Phys. J.* **C71** (2011) 1554, doi:10.1140/epjc/s10052-011-1554-0, 10.1140/epjc/s10052-013-2501-z, arXiv:1007.1727.

[50] F. Garwood, "Fiducial Limits for the Poisson Distribution", *Biometrika* **28** (1936) 437–442, doi:10.1093/biomet/28.3-4.437.